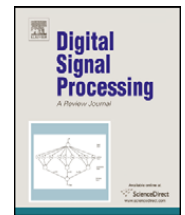Contents lists available at ScienceDirect

Digital Signal Processing

www.elsevier.com/locate/dsp

Wavelet based local tomographic image using terahertz techniques

Xiaoxia Yin [a,*], Brian W.-H. Ng [a], Brad Ferguson [a,b], Derek Abbott [a]

[a] *Center for Biomedical Engineering and School of Electrical & Electronic Engineering, The University of Adelaide, SA 5005, Australia*
[b] *Tenix – Electronic Systems Division, 2nd Avenue, Technology Park, Mawson Lakes, SA 5095, Australia*

ARTICLE INFO

ABSTRACT

Terahertz computed tomography has been developed based on coherent THz detection and filtered back projection (FBP) algorithms, which allows the global imaging of the internal structure and extraction of the frequency dependent properties. It offers a promising approach for achieving non-invasive inspection of solid materials. However, with traditional CT techniques, i.e. FBP algorithms, full exposure data are needed for inverting the Radon transform to produce cross sectional images. This remains true even if the region of interest is a small subset of the entire image. For time-domain terahertz measurements, the requirement for full exposure data is impractical due to the slow measurement process. This paper explores time domain reconstruction of terahertz measurements by applying wavelet-based filtered back projection algorithms for recovery of a local area of interest from terahertz measurements within its vicinity, and thus improves the feasibility of using terahertz imaging to detect defects in solid materials and diagnose disease states for clinical practise, to name a few applications.

© 2008 Elsevier Inc. All rights reserved.

1. Introduction

Terahertz radiation (T-rays) is a collective term to describe the part of the electromagnetic spectrum from 0.1 to 10 THz [22]. The application of THz time domain spectroscopy (THz-TDS) in fields such as biomedical engineering, security and material science is attractive owing to two intrinsic properties: a non-ionising nature and the ability to penetrate dry, non-polar and non-metallic materials [6]. Compared to X-rays, T-rays have the safety advantage of being non-ionising. Additionally, compared to traditional X-ray techniques, T-ray 3D imaging uses coherent tomography, which allows access to both phase and amplitude information of an object. Generally, X-rays perform best for dense materials (e.g. for imaging skeletal features), whereas T-rays are complimentary and better suited for surface soft tissue. For over a decade, ultrashort terahertz pulses have been investigated for applications including measuring the optical properties of materials in the submillimetre wavelength regime, tissue burn diagnostics and DNA analysis [9,20], to name but a few examples.

In recent years a number of methods for 3D imaging with terahertz radiation have been proposed and demonstrated [16]. Most schemes using THz pulsed imaging (TPI) are based on the extraction of material parameters [6]. It can be reconstructed by representing any desired aspect of the measured waveforms, including amplitude, phase, time-of-flight, or their combinations [15]. Currently, there are several types of terahertz tomography [23]: (i) tomography with a Fresnel Lens (TFL), demonstrated by Wang and Zhang [21]; (ii) multistatic imaging techniques, which apply multiple detectors that are positioned to capture the scattered radiation at different angles [18]; (iii) terahertz holography and terahertz diffraction tomography, as an extension of terahertz imaging techniques, have been explored by different terahertz groups [2,16]. In

---

* Corresponding author.
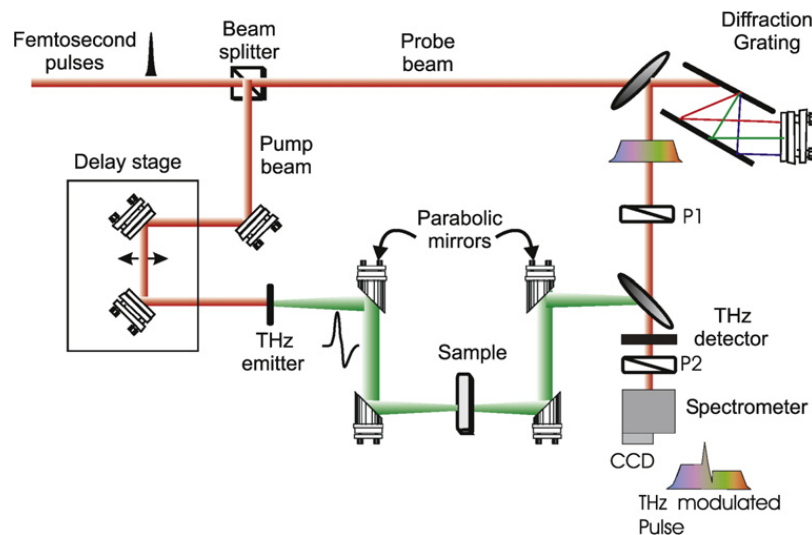*E-mail address:* xxyin@eleceng.adelaide.edu.au (X. Yin).

Fig. 1. A chirped probe pulse terahertz imaging system is used to realise terahertz CT imaging. After [6]. In practise, the sample is placed on a rotational stage.

summary, the different types of terahertz tomography are capable of mapping 2D and 3D distributions of scattering objects, but with a constraint to image the shape profile of the target object [4].

This paper for CT reconstruction is motivated by terahertz TDS imaging mechanisms and focuses on terahertz CT imaging with reduced projection measurements. The main goal of THz local reconstruction is to present a wavelet based reconstruction algorithm for terahertz computed tomography and to show how this algorithm can be used to rapidly reconstruct a given region of interest (ROI) with a reduction in the measurements of terahertz responses, compared with a standard reconstruction. The current algorithm provides new insight into the relationship between local reconstruction, local projection, and the resolution of terahertz coherent tomography. This algorithm uses wavelet techniques and operates by generating the approximation and detail images separately, with the final reconstruction found by inverse wavelet transform. The algorithm reconstructs (i) a centre region with radius of 16 pixels in a 100×100 pixel image to within 26% maximum relative error using 46% of full data; (ii) an off-centre region with radius of 30 pixels in a 100×100 image to within 24% maximum relative error using 66% of full data. It should be noted that the full data mentioned above, also called full tomographic data, is defined as the projection data that covers the entire sample. This is different to the local (tomographic) data, which is defined as the projection data that only covers the target region of interest. Since the current reconstruction algorithm is the first attempt in terahertz tomographic imaging, we believe it is valuable start even if the relative error is somewhat high.

The current algorithm achieves the reconstructed approximate and detailed portions of an image via conducting back projection with ramp filtered scaling and wavelet functions. Compared to previous algorithms in terahertz computed tomography [5,16], the current reconstruction algorithm accelerates terahertz image scanning and reduces computational complexity by considering only a small number of projections passing through the ROI and its immediate neighborhood. Therefore, it is computationally more efficient. Uniform exposure is adopted at all angles for simpler implementation in the hardware setup. Reconstruction ability for off-centred and centred regions of interest are also explored.

This paper consists of six sections. Section 2.2 introduces a terahertz functional imaging system. Section 3 is an overview of the non-locality of the Radon transform—this is important because we review the difference between the conventional Radon transform reconstruction and our modified Radon transform for local tomography. After reviewing the basics of the wavelet transform, Section 3 continues to describe a full-data reconstruction technique based on the wavelet transform. Section 4 then discusses the implementation of this method; Section 5 presents the tomographic results. Finally, Section 6 concludes the paper with a summary of the work and recommendation for future direction of this work.

2. A brief introduction to terahertz imaging

In this section, we introduce a chirped pulsed imaging setup, describe the grating pair functions and discuss the effect that the grating pair has on the path of the individual diffracted beams.

2.1. The experiment setup for terahertz imaging

A chirped terahertz time domain spectroscopy scanned imaging system is used for making the image data measurements; such a system is illustrated in Fig. 1. The target is mounted on a motion stage so that the object can be rotated and linearly moved. As seen in Fig. 1, terahertz pulsed imaging (TPI) is achieved by repeating pulsed terahertz measurements in a 2D raster scan. The ultrafast pulsed laser beam is split into separate probe and pump beams. The path length of the pump
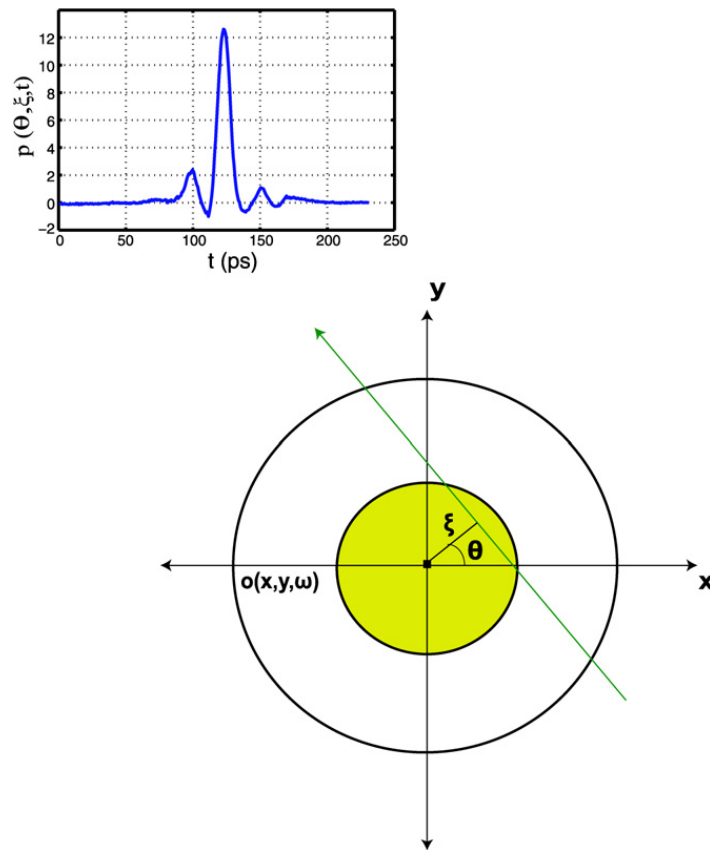
Fig. 2. Illustration of two sets of coordinate systems for the reconstructed terahertz CT. A typical terahertz pulse spectrum is shown as a function of time t in the inset. After [6].

beam is adjusted by a delay stage, then transmitted through a chopper and enters one of the optical rectification crystals, which operates as a terahertz emitter. One pairs of parabolic mirrors are employed to focus T-rays onto a sample. The T-rays emerging from the sample are adjusted again by another pair of parabolic mirrors, then being combined with the probe beam co-linearly. For the current chirped pulsed imaging system, the optical probe beam is linearly chirped by a grating pair. The grating pair encodes the chirped signal in space and allows an electro-optic crystal to sample the terahertz temporal profile simultaneously. The grating pair (grating constant 10 μm) is setup so that the grating separation is 4 mm and the angle of incidence is 51°, giving a chirped probe pulse width of 21 ps. The probe pulse is linearly polarised by P1 and the polarisation modulation is converted to an amplitude modulation by polariser P2 whose polarisation is perpendicular to P1. On transmission through the sample the THz radiation and optical probe beam are reflected by and transmitted through an ITO THz mirror, separately. The detector crystal produces optical outputs that are proportional to the terahertz response. A CCD spectrometer is used for signal measurement. For the current reconstruction, we employ coherent spectrometry with a spectral resolution of 17 GHz and a detection lock-in amplifier time constant of 10 ms.

This current terahertz imaging setup achieves point to point detection. A linearly moving stage enables parallel scanning and a rotating stage allows projections of an object to be taken at a number of projection angles and distance offset from the centre of the rotation. These variables are denoted θ and ξ, respectively, and are illustrated in Fig. 2. Adding to these two spatial variables is the time variable which is associated with the transient terahertz pulse. The measurements gathered from such a setup is organised as a three-dimensional (3D) dataset, indexed by the variables (θ, ξ, t). The optical properties of the material are extracted in the Fourier domain. In this domain, the tomographic inversion process takes place, to yield a final reconstruction as a function of the variables (x, y, ω). The processing required to effect this transformation is described in Section 3.2 below.

2.2. Characteristics of diffraction grating pair

A typical parallel grating pair used to create a chirped pulse. A chirped pulse imaging system greatly accelerates the image process. The different wavelength components of the incident pulse traverse different path lengths due to the variation in first order diffraction angle with wavelength.
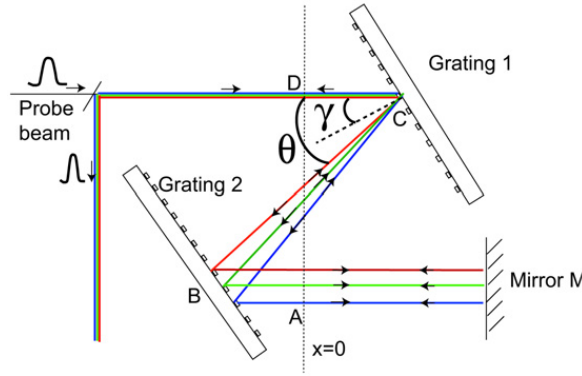
Fig. 3. The geometry of a diffraction grating for chirped pulsed compression. The grating is used to impart a linear chirp to a laser pulse. The mirror M reflects the beam back into the grating pair. The optical path length is greater for longer wavelengths. The angle of incidence is γ and θ is the angle between incident and diffracted rays.

According to Treacy et al. [19], for a parallel grating pair, if light of wavelength λ is incident on a grating with grating constant d at an angle γ (relative to the grating normal), and a wavelength-dependent angle θ is the angle between incident and diffracted rays, then the ray path length (ABCD in Fig. 3) is given by

$$p = b(1 + \cos\theta) = c\tau, \tag{1}$$

where $b = G\sec(\gamma - \theta)$ is a slant separation between the two gratings, if G is the perpendicular distance between the gratings, and τ labels group delay.

The variation of group delay with wavelength is defined as

$$\delta\tau = \frac{b(\lambda/d)\delta\lambda}{cd[1 - (\lambda/d - \sin\gamma)^2]}. \tag{2}$$

This is an optical element used to see the group delay dispersion. The group velocity dispersion (GVD) indicates the group delay dispersion per unit length, which represents the phenomenon of the frequency (or wavelength) dependent group velocity of a wave. Group velocity reflects the changes of the wave in propagated amplitude (known as the envelope of the wave). It is important factor in affecting temporal pulse broadening.

The relation between γ and θ for first-order diffraction is

$$\sin(\gamma - \theta) + \sin\gamma = \frac{\lambda}{d}; \tag{3}$$

here d is the grating constant. Combined with Eq. (1), it is concluded that the optical path through grating pair is longer for the longer wavelength of waves than that of the shorter ones.

Fig. 3 shows a simplified pulse compressor via a pair of parallel gratings. The mirror M reflects the beam back into the grating pair, and the pair of parallel and face-to-face gratings is used to diffract light twice, so that the outgoing waves are parallel to, but laterally displaced from, the incoming waves. That is, pulse stretching is essentially the reverse of the pulse compression.

According to the grating equation, the longer wavelength light (top, red line) is diffracted through a smaller angle θ than the shorter wavelength light (middle, green and bottom, blue line), so that the red light strikes the second grating to the left of the green while the blue light is to the right of the green. As a result, the total free-space path taken by a red ray is longer than that of a green ray, which is in turn longer than the blue ray's path. It turns out to be that the output from the grating is a pulse with a longer pulse duration and a wavelength that varies linearly with time. The negative group velocity is provided via the pair of parallel gratings. Since the input pulse is positively chirped travels through the gratings, the output pulse becomes shorter due to partial cancellation of the positive GVD effect by the negative GVD of the gratings.

Electro-optic (EO) detection of a terahertz pulse using a chirped probe pulse was first demonstrated by Jiang and Zhang [10]. This novel technique allows the full T-ray waveform to be measured simultaneously rather than requiring a stepped motion stage to scan the temporal profile. This provides a significant reduction in the acquisition time and greatly extends the applicability of T-ray systems in situations where the sample is dynamic or moving. Indeed, single shot measurements have been demonstrated for measuring a T-ray pulse using a single femtosecond light pulse [11].

However, this method degrades the SNR by spreading the available THz power over multiple pixels and diffraction effects can corrupt the temporal measurements. To avoid these additional concerns, the current experiment concentrates on the use of scanned imaging by focusing the THz pulses to a point and raster scanning the target.

3. Methodology

3.1. An overview of CT and terahertz CT

Computed tomography produces sectional images of an object, which is based on the assumption that the image to be reconstructed belongs to an identifiable ensemble of similar images [8]. The filtered back projection algorithm, is often used in the calculation of the inverse Radon transform [6,12,22], which reconstructs a target object. Typically, the quantities obtained are the object's frequency dependent optical properties, such as the refractive index.

Conventionally, a filtered back projection algorithm begins with a collection of *sinograms* obtained from projection measurements. A sinogram is a collection of points in a projection space, which reflect projection geometric paths in an image space. A sinogram is generated using Radon transform data, denoted below by $\Re$ and is simply a collection of the projections at all the projection angles. A 1D projection operation at each projection angle is a linear integral of the image intensity along projection offset ξ, which satisfies the following equation:

$$s(\xi, \theta) = \int o(x, y) \, d\xi = \Re(o) \tag{4}$$

where all points on projection offset ξ satisfy the equation: $x \cos\theta + y \sin\theta = \xi$ and o denotes the measured image intensity of a target object, which is a function of pixel position in an x and y plane.

The filtered back projection algorithm for terahertz CT reconstruction is expressed as follows:

$$I(x, y) = \int_0^\pi \left[\int_{-\infty}^\infty S(\theta, \beta) |\beta| \exp[i2\pi\beta\xi] \, d\beta \right] d\theta, \tag{5}$$

where $S(\theta, \beta)$ is the spatial Fourier transform of the parallel projection data, defined as

$$S(\theta, \beta) = \int_{-\infty}^\infty s(\theta, \xi) \exp[-i2\pi\beta\xi] \, d\xi; \tag{6}$$

here $s(\theta, \xi)$ is the measured projection data, β is the spatial frequency in the ξ direction. It should be noted that the operation of the ramp filter $|\beta|$, as illustrated in Eq. (5), is equivalent to a differentiation followed by a Hilbert transform, which introduces a discontinuity in the derivative of the Fourier transform at zero frequency. This means that the traditional Radon transform inversion does not allow a local reconstruction of a CT image. This is the reason why a wavelet based algorithm is used in this paper.

3.2. Calculation of terahertz parameters for reconstruction of terahertz CT

One of the advantages that terahertz CT has over X-ray CT is that $s(\theta, \xi)$ may be one of several parameters derived from terahertz pulses. Fundamentally, a terahertz CT setup is capable of measuring the transmitted terahertz pulse as a function of time t, for a given projection angle and projection offset. In principle, terahertz sinograms can be obtained in both time and frequency domains. In this paper, we illustrate time domain signogram for terahertz CT.

The time domain signogram is based on the assumption that the target is dispersionless and therefore the THz pulse shape is unchanged after propagation through the target apart from attenuation and time delay. A reference terahertz pulse $p_r(t)$ is measured without the target in place. To estimate the phase shift t of a terahertz pulse $p_s(t)$, the two signals are resampled at a higher rate using bandwidth-limited interpolation.

$$p_{\text{ref}}(m) = \sum_{t=-\infty}^\infty p_r(t) \, \text{sinc}\left[\frac{1}{q}(m - qt) \right], \tag{7}$$

$$p_{\text{sample}}(m) = \sum_{t=-\infty}^\infty p_s(t) \, \text{sinc}\left[\frac{1}{q}(m - qt) \right]. \tag{8}$$

The two interpolated signals are then cross-correlated, and the maximised cross-correlation product at each angle as the lag is taken as the estimation of the phase delay of $p_s(t)$. Mathematically, this process is described by

$$R_{p_s p_r}[m] = p_{\text{sample}}(m) \otimes p_{\text{ref}}(m) = \sum_{t=-\infty}^\infty p_{\text{sample}}(k) p_{\text{ref}}(k - m),$$

$$T_d = \langle p_{\text{sample}} \otimes p_{\text{ref}}(m) \rangle_{\text{maxlag}}, \tag{9}$$

where T_d is to estimate the delay time of terahertz phase, $p_{\text{sample}}(m)$ and $p_{\text{ref}}(m)$ are equal to $p_d(t)$ and $p_i(t)$ after interpolation by a factor of q. For the current experiment, $q = 2$ and $m = 301 \times 10 = 3010$. As shown in Eq. (9), the operator R denotes the cross-correlation and $\langle f(t) \rangle_{\text{maxlag}}$ denotes calculating the value of t at which the function f takes its maximum.
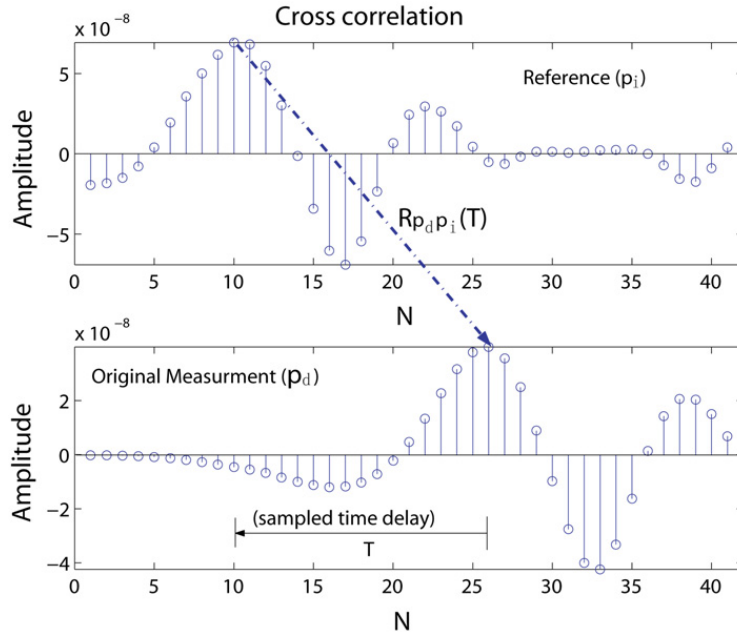
Fig. 4. Illustration of the cross-correlation algorithm with the truncated projection of cylinder data sets after interpolation for clarity.

Timing sinogram can be calculated based on the following equation:

$$p_{\text{time}} = \int_{L(\theta,\xi)} T_d \, dr = \Re\{T_d(r)\}; \tag{10}$$

here p_{time} denotes the sinogram image in the time domain, recovered from the maximum time delay.

Fig. 4 illustrates the cross-correlation algorithm. The truncated terahertz projection response shown was interpolated and cross correlated with the reference pulse. The lag T at which the cross-correlation is maximised provides an accurate estimate of the delay between the two pulses. The algorithm is applied to cylinder data for terahertz CT reconstruction in Section 5.

3.3. Two-dimensional wavelet-based CT reconstruction

3.3.1. Two-dimensional wavelet transform (2D DWT)

Wavelet transforms play an important role in many image processing algorithms. Fundamentally, wavelet decomposition corresponds to a multiresolution analysis of a signal that carries the advantage of greatly improved joint time–frequency localisation over Fourier-based techniques. Following the early works in wavelet-based tomography [3,17], the discrete version of the wavelet transform (DWT) is used in this paper. Compared with other formulations, DWT offers computational efficiency since they are nearly always implemented with short length digital filters. In one dimension, the famous Mallat's pyramid algorithm allows the multiresolution decomposition coefficients at any scale to be calculated from coefficients at lower scales, by cascaded filtering with a pair of FIR low-pass (h_0) and high-pass (h_1) filters. These filters are alternatively known as a pair quadrature mirror filters. The filters h_0 and h_1 characterise the scaling function and wavelet functions, respectively. In two dimensions, the 2D multiresolution coefficients are calculated by applying Mallat's algorithm separately to the rows and columns [7]. The corresponding approximate and detailed coefficients at scale $j+1$ are computed from the approximate coefficients at scale j, $c_j(m,n)$ by the following equations:

$$c_{j+1}(k,l) = \sum_{m,n} h_0(2k-m)h_0(2l-n)c_j(m,n), \tag{11}$$

$$d_{j+1}^H(k,l) = \sum_{m,n} h_0(2k-m)h_1(2l-n)c_j(m,n), \tag{12}$$

$$d_{j+1}^V(k,l) = \sum_{m,n} h_1(2k-m)h_0(2l-n)c_j(m,n), \tag{13}$$

$$d_{j+1}^D(k,l) = \sum_{m,n} h_1(2k-m)h_1(2l-n)c_j(m,n), \tag{14}$$

where the sequences d_{j+1}^H, d_{j+1}^V and d_{j+1}^D correspond to horizontal, vertical, and diagonal high frequency subbands, respectively, while c_{j+1} corresponds to coefficients representing low frequency information [14]. Here, h_0 and h_1 are a suitable
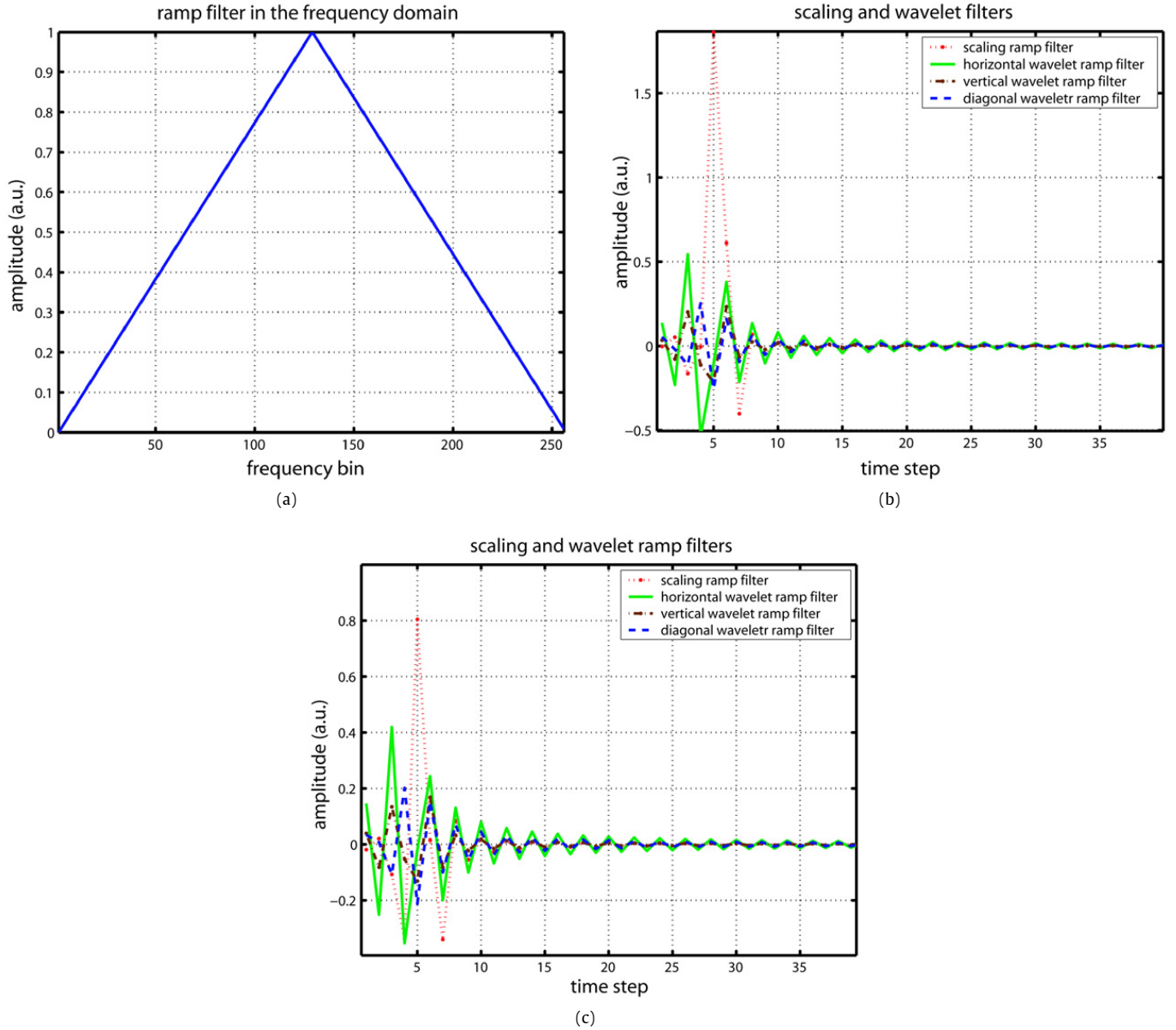
Fig. 5. (a) Illustration of a traditional ramp filter. (b) and (c) are the illustration of the scaling and wavelet ramp filters at the sixth projection angle (43.2°) using BiorSplines 2.2 wavelet, respectively.

pair of low-pass and high-pass filters. In our current experiment, symmetric (linear phase) filters are used for the analysis and synthesis of the tomographic reconstruction. Let h_0, h_1, denote a pair of linear phase low- and high-pass filters and $\tilde{h}_0$, $\tilde{h}_1$ denote the corresponding reconstruction filters. The discrete approximation at scale j can be obtained by combination of the details and approximation at scale $j + 1$ by

$$c_j(k, l) = \sum_{m,n} \tilde{h}_0(k - 2m)\tilde{h}_0(l - 2n)c_{j+1}(m, n) + \tilde{h}_0(k - 2m)\tilde{h}_1(l - 2n)d^H_{j+1}(m, n)$$

$$+ \tilde{h}_1(k - 2m)\tilde{h}_0(l - 2n)d^V_{j+1}(m, n) + \tilde{h}_1(k - 2m)\tilde{h}_1(l - 2n)d^D_{j+1}(m, n). \tag{15}$$

Our method is to focus the wavelet application on recovering local images from wavelet approximate and detail coefficients. In order to support the reconstructed filter for the recovery of the local target area, the calculation of these reconstructed coefficients includes the region of interest and a small margin area immediately surrounding the ROI.

3.3.2. Two-dimensional wavelet-based CT reconstruction

This section briefly describes an algorithm, which is applied to obtain the wavelet coefficients of a function on $\mathbb{R}^2$ space, based on Radon transform data. In this algorithm, the wavelet coefficients are calculated locally, allowing the reconstruction to yield local computed tomography [17]. The main formulas for 2D DWT, on projection data, for the reconstruction of a CT image are introduced, which are realised via performing separate wavelet transforms on 1D projection data.

The filtered back projection algorithm for terahertz CT reconstruction is expressed as follows:

$$I(x, y) = \int_0^\pi \left[\int_{-\infty}^\infty S(\theta, \beta) |\beta| G_j(\beta \cos\theta, \beta \sin\theta) \exp(i2\pi\beta\xi) \, d\beta \right] d\theta, \tag{16}$$

where $S(\theta, \beta)$ and $G_j(\beta_1, \beta_2)$ are the spatial Fourier transforms of $s(\theta, \xi)$ and g_j (a wavelet ramp filter in the time domain), respectively. From Eq. (16), it is clear that image reconstruction can be obtained from the conventional Radon transform inversion process, but with the ramp filter $|\beta|$ replaced by the wavelet ramp filter $|\beta| G_j(\beta \cos\theta, \beta \sin\theta)$. For the separable wavelet bases under our consideration, the approximate and detail coefficients can be calculated from the projection data via Eq. (16), with $G_j(a, b)$ in the inner integral replaced by $\Phi_j(a, b) = \hat{\phi}_j(a)\hat{\phi}_j(b)$, $\Psi_j^H(a, b) = \hat{\phi}_j(a)\hat{\psi}_j(b)$, $\Psi_j^V(a, b) = \hat{\psi}_j(a)\hat{\phi}_j(b)$, and $\Psi_j^D(a, b) = \hat{\psi}_j(a)\hat{\psi}_j(b)$, respectively, where $a = \beta\cos\theta$, $b = \beta\sin\theta$, and the caret sign indicates the Fourier transform of the relative functions. For instance, the approximate coefficients are obtained by

$$c_j(k, l) = \int_0^\pi \left[\int_{-\infty}^\infty S(\theta, \beta) |\beta| \Phi_{2^j} \cdot (\beta\cos\theta, \beta\sin\theta) \exp(i2\pi\beta\xi) \, d\beta \right] d\theta. \tag{17}$$

The detail coefficients can found in a similar way as follows:

$$d_j^i(k, l) = \int_0^\pi \left[\int_{-\infty}^\infty S(\theta, \beta) |\beta| \Psi_{2^j}^i(\beta\cos\theta, \beta\sin\theta) \exp(i2\pi\beta\xi) \, d\beta \right] d\theta, \tag{18}$$

where $i = H, V, D$ for the horizontal, vertical and diagonal detail coefficients, respectively. This means that the filtered back projection method can be applied to the wavelet transform of the projections for image recovery, while the ramp filter is replaced by

$$\begin{cases} H_\theta^C = |\beta| \Phi_{2^j}(\beta\cos\theta, \beta\sin\theta) = |\beta| \Phi_{2^j}(\beta\cos\theta)\Phi_{2^j}(\beta\sin\theta), \\ H_\theta^{D^H} = |\beta| \Psi_{2^j}^h(\beta\cos\theta, \beta\sin\theta) = |\beta| \Phi_{2^j}(\beta\cos\theta)\Psi_{2^j}(\beta\sin\theta), \\ H_\theta^{D^V} = |\beta| \Phi_{2^j}^V(\beta\cos\theta, \beta\sin\theta) = |\beta| \Psi_{2^j}(\beta\cos\theta)\Phi_{2^j}(\beta\sin\theta), \\ H_\theta^{D^D} = |\beta| \Psi_{2^j}^d(\beta\cos\theta, \beta\sin\theta) = |\beta| \Psi_{2^j}(\beta\cos\theta)\Psi_{2^j}(\beta\sin\theta), \end{cases} \tag{19}$$

where H_θ^C and $H_\theta^{D^i}$ ($i = H, V, D$) are called scaling and wavelet ramp filters, respectively. Fig. 5a illustrates the scaling and wavelet ramp filters at the sixth projection angle (43.2°) using BioSplines 2.2 bi-orthogonal wavelet.

For the current image reconstruction, only one 2D wavelet transform step is used. This is because the single level decomposition of scaling and wavelet ramp filters allows clear reconstruction of an image in the ROI and it avoids more computational complexity due to greater levels of WT [3,17]. The wavelet reconstruction formula in Eq. (16) allows for such reconstruct by setting $j = 1$.

3.4. Local reconstruction using wavelets

A significant characteristic of most wavelets are their large number of vanishing moments. Hilbert transforms of functions with many vanishing moments have been shown to decay very rapidly at infinity [3]. In other words, a wavelet function with compact support allows a local basis to mostly maintain its localisation after Hilbert transformation [1,3]. Figs. 5a–5c illustrate the ramp filter over the full frequency domain, the BiorSplines bi-orthogonal scaling and wavelet filters and the ramp filtered version of the BiorSplines bi-orthogonal wavelet and scaling filters, where the horizontal axis represents the number of time or frequency samples, and the vertical axis represents the relative amplitude. Fig. 5c essentially shows the compact support after applying Hilbert transforms. Therefore, the wavelet and scaling coefficients for some wavelet basis can be calculated after applying the projections passing through the region of interest plus a margin for the support of the wavelet and scaling ramp filters. These reconstructed coefficients, in this experiment, are then directly applied to the inverse wavelet transforms for terahertz image reconstruction.

3.4.1. Error analysis
As the Hilbert transform is non-local, in order to recover an image in the local region of interest, the non-local data that is outside the ROI have to be considered for an accurate local reconstruction. An upper bound for the reconstruction error, denoted by E_{ub} can be calculated and therefore the relative error E_r is used in this paper for evaluation of the current reconstruction. The principle for error analysis [17] is to consider the measured projections divided into two parts: one is for the region of exposure and another is its complement. The full details of the error analysis can be found in [17]; here we will present a brief summary so this paper can be read independently.

We consider the original measurement of target image $I(x, y)$ with a support centred at the origin and within a radius of 1 unit. Based on the Cauchy–Schwartz inequality and the assumption that $|s_{\theta_k}| \leqslant 2\max|I(x, y)|$, where the support of

$I(x, y)$ is within a radius of 1, $|s_{\theta_k}|$ is the projection at the kth projection angle, the relative error E_r can be calculated via dividing the upper bound of the reconstructed error E_{ub} by the maximum intensity of the support $\max |I(x, y)|$. The relative error calculated in the frequency domain satisfies the following equation:

$$I(x, y) = \frac{2\sqrt{2}\pi}{k} \frac{\sqrt{R - r_e}}{R} \cdot \sum_{k=1}^{K} \left(\sum_{|n|=-R}^{R} \left| [\bar{H}_{\theta_k}(n) - \bar{H}_{\theta_k}^T(n)] \right|^2 \right)^{1/2}, \tag{20}$$

where $\bar{H}_{\theta_k}$ is the inverse Fourier transform of H_{θ_k} and H_{θ_k} can be replaced by the ramp filter $|\beta|$.

The truncated filter $H_{\theta_k}^T$ is defined as

$$H_{\theta_k}^T(n) = \begin{cases} H_{\theta_k}(n) & \text{if } |n| < r_e - r_i, \\ 0 & \text{otherwise;} \end{cases} \tag{21}$$

here r_e and r_i are the radii corresponding to ROI and ROE, both of which are centred at the origin of the image.

The upper bound of the relative error in the reconstructed sinogram of scaling and wavelet coefficients can be obtained by replacing H_{θ_k} in Eq. (20) with the filters defined in Eq. (19) and multiplying by a normalising factor. Equation (22) represents the relative error in the reconstructed image from approximate reconstruction coefficients,

$$\left| E_r(x, y) \right| = N_{I_{g,l_C}} \cdot \frac{2\sqrt{2}\pi}{k} \frac{\sqrt{R - r_e}}{R} \cdot \sum_{k=1}^{K} \left(\sum_{|n|=-R}^{R} \left| [\bar{H}_{\theta_k}(n) - \bar{H}_{\theta_k}^T(n)] \right|^2 \right)^{1/2}, \tag{22}$$

where $N_{I_{g,l_C}}$ is the normalised scale factor of an image in relation to approximate reconstruction coefficients, which is calculated via dividing maximum intensity of global reconstruction, denoted by $I_r(x, y)$, by maximum intensity of local reconstruction regarding approximate wavelet coefficients, denoted by $I_{\text{local}}^C(x, y)$. The scale factor is as follows,

$$N_{I_{g,l_C}} = \frac{\max |I_r(x, y)|}{\max |I_{\text{local}}^C(x, y)|}. \tag{23}$$

For convenience, the error calculation in the current experiment is limited to the error of the approximate image reconstruction. Most of the energy of an image is compacted to the approximate image, so the error estimate for this image gives a good indication of the overall error.

4. Implementation

4.1. Practical consideration

The current research based on terahertz imaging is inspired by the work of Rashid-Farrokhi et al. [17]. In this work, we experiment with the 2D wavelet technique using terahertz tomographic data by modifying the measured projections. As we show later, this modification involves an extrapolation technique to avoid edge effects due to sinogram truncation. It is observed that approximate coefficients of a scaling function shows good localised features in the local reconstruction using our algorithm, where the reconstructed intensity of an image varies greatly between different target materials. It should be noted that, in the application of terahertz data for local reconstruction, it is found that the intensity at the edges of the region of exposure (ROE) in terahertz projections, where non-local data is set to zero, varies considerably after filtering with either the traditional ramp filter or the modified scaling and wavelet ramp filters.

In local reconstruction, artifacts are common close to the boundary of the ROE, which can readily be observed in the application to terahertz CT data. In this paper, terahertz data measured from a simple structure: a cylinder with holes inside is considered for the current reconstruction. The sample consists of 101 projections at each of 25 projection angles covering a $180°$ projection area in a 100×100 image. In our experiment, a 196×196 pixel image is also obtained after taking the inverse wavelet transform for clarity.

In the current wavelet based reconstruction, if without a down sample procedure, the relative reconstruction size is 196×196. Two situations are analysed for this target sample: (i) an ROE of diameter 42 pixels at the centre of the image and (ii) an ROE of diameter 67 pixels offcenter to the image. Fig. 6a shows sharp variations along the boundaries of the ROE after applying wavelet ramp filters and ramp filter, respectively, on each of the 1D projections, which result in an image appearing relatively weakened intensity compared to a large constant bias that exists along the reconstructed edges in the region of interest. The constant extrapolation we use was first suggested by Rashid-Farrokhi et al. [17]. In order to fit terahertz signals, the current algorithm replaces r_e with $(r_e - r_a)$ to diminish the artificial effect along the edge of ROE, where r_a is the radius of the region of artifacts (ROA), which is an annulus co-centred with the ROE.

Fig. 6b shows the extrapolated projection at the 25th projection angle after the application of a scaling ramp filters and a ramp filter. The extrapolated projection removes spikes at the edge of the ROE. The extrapolation algorithm is suitable to the reconstruction of an image at the off-centre area. In order to recover the cross-sectional image in the region of interest, the values of the sinograms outside of the ROE are set to zero. The traditional filtered back projection formulas and wavelet based reconstruction are applied to the remaining projections, respectively for analysis and comparison.
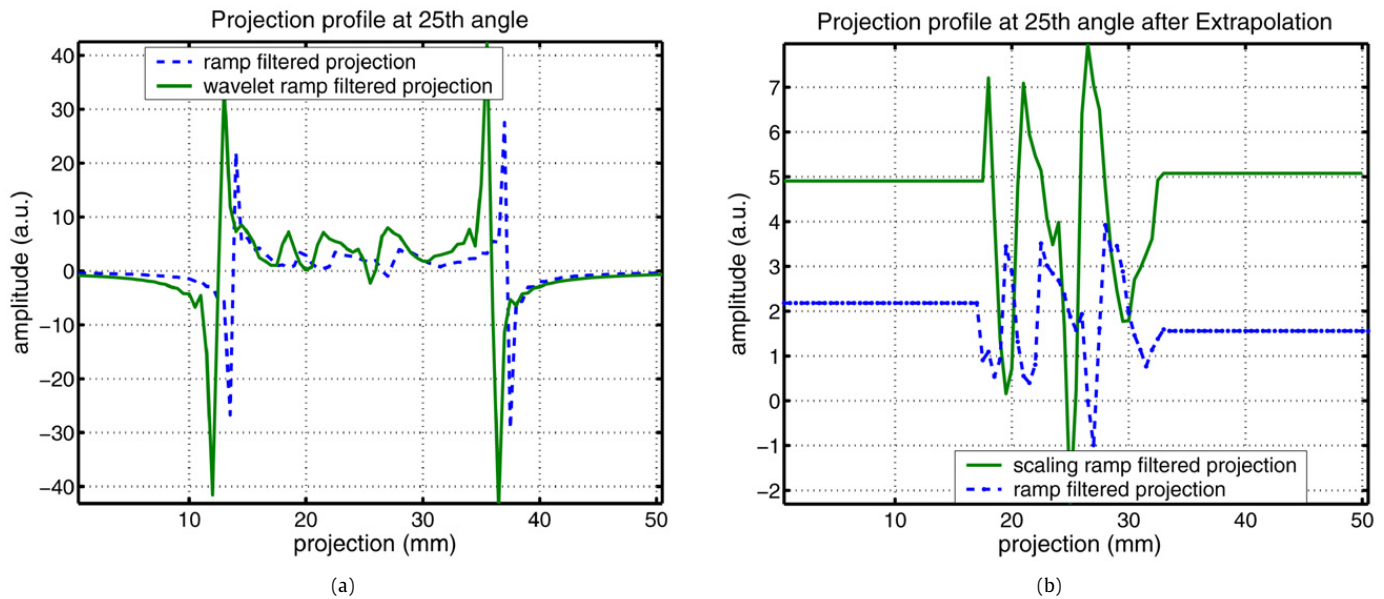
Fig. 6. (a) Projection filtered by a scaling ramp filter and a traditional ramp filter, respectively. (b) Projection extrapolation outside the ROI after filtered projections.

It should be noted that there are phase shifts observed in Fig. 6, which are caused by the convolution of the ramp filter with the wavelet/scaling filter(s). However, since the wavelet and scaling filters are designed to satisfy the perfect reconstruction property, these shifts cancel out when the inverse 2D DWT is applied to yield the overall CT reconstruction.

However, according to the following local resultant reconstruction examples, it is observed that an approximate image has better resultant reconstruction than using inversed wavelet reconstructed subimages, in the current algorithm related to wavelet based reconstruction. Consequently we only consider the approximate image reconstruction to evaluate the algorithm validation. As we mainly deliver local information for the back projection, the wavelet and scaling ramp filters show essentially same support. But we have to recognise that having a scaling-only reconstruction means we theoretically lose some accuracy in locating any edges.

4.2. Algorithm summary

The wavelet based reconstruction algorithm assumes an image support of radius R, and the radius of the ROI is r_i. A radius $r_e = r_i + r_a$ is exposed, where r_a is the extra margin with related to radius of ROA, which is produced by applying wavelet filters on the project data. The algorithm is summarized as follows:

(1) The original projections are calculated from time or frequency parameters from terahertz measurements.
(2) The region of exposure is truncated for the reconstruction of an image in the region of interest.
(3) The region of exposure of each projection is filtered by modified wavelet filters at all projection angles. This step is to recover an image related to wavelet detailed coefficients.
(4) The region of exposure of each projection is filtered by modified scaling filter at all projection angles, which will lead to the recovery of the approximation sub-image.
(5) The projections from step (4) are extrapolated with the edge values for locations outside the ROE, in order to limit artifacts at the ROE boundaries.
(6) Filtered projections obtained in steps (3) and (4) are back projected to every other point to obtain the approximate and detail at the higher resolution.
(7) The image is reconstructed from the wavelet and scaling coefficients via a conventional inverse DWT.

5. Reconstruction results

5.1. Global reconstruction

The first simulation results show the wavelet-based reconstruction when the full tomographic data is available. In such a case, the wavelet-based technique should produce identical results to the traditional filtered backprojection algorithm. In our experiment, a 196×196 pixel image of the polystyrene target is recovered from the wavelet and scaling coefficients using global data, shown in Fig. 7a, without decomposition in the inverse wavelet transform for clarity and comparison. Each measured terahertz pulse is a function of time with 401 samples at uniform time intervals of 0.067 ps. Wavelet and
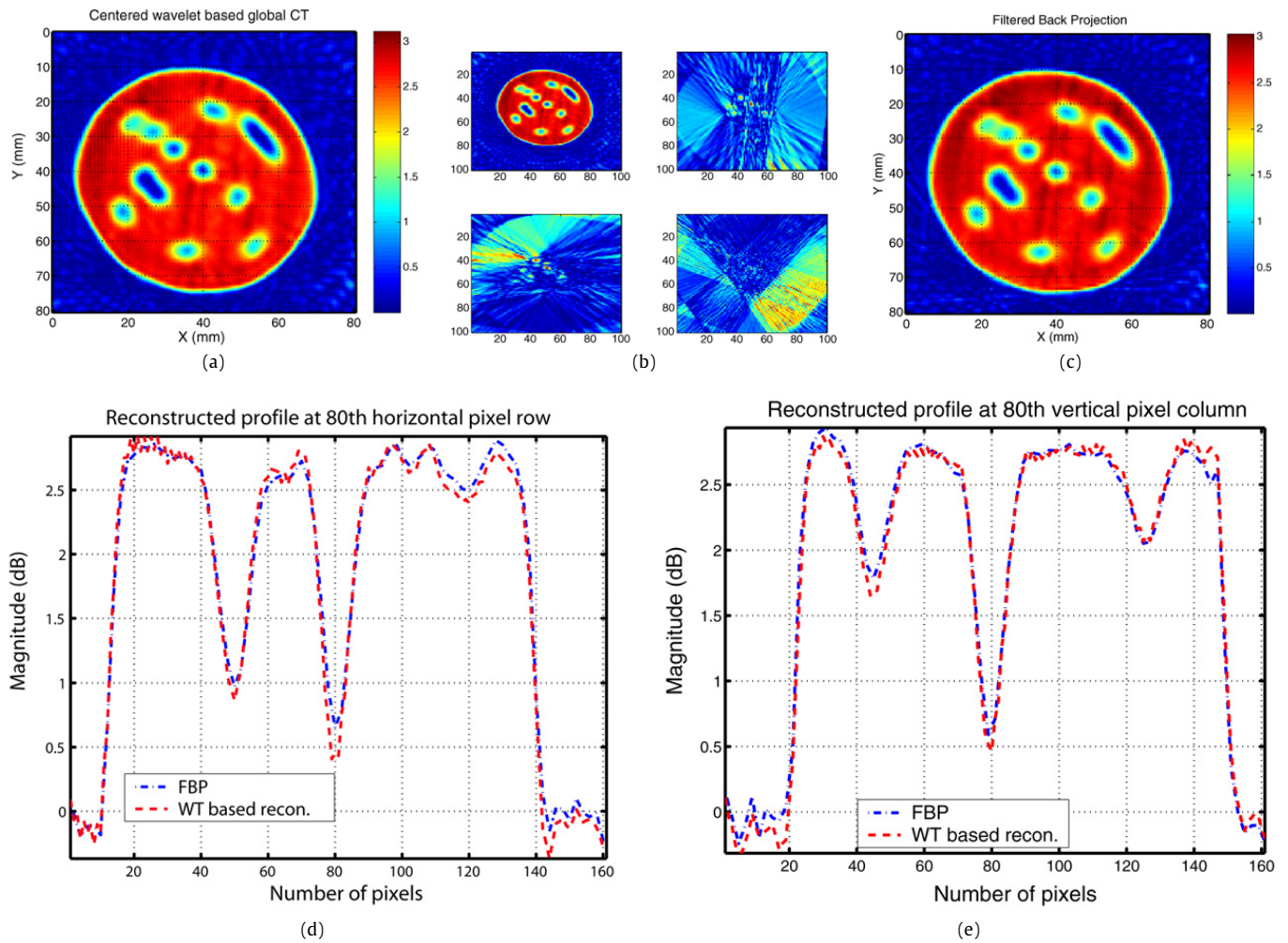
Fig. 7. (a) A 196 × 196 pixel image of the polystyrene target is recovered from the wavelet and scaling coefficients using global data, without decomposition. (b) Wavelet and scaling coefficients after back projection. (c) A 196 × 196 pixel image of the polystyrene is reconstructed using traditional filtered back projection. (d) Reconstructed profiles at the 80th row (40 mm at y axis). (e) Reconstructed profiles at the 80th column (40 mm at x axis).

scaling coefficients after back projection are shown in Fig. 7b, where the BioSpline 2.2 biorthogonal basis is used. The quality of the reconstructed image is, as expected, almost indistinguishable from the reconstruction using traditional filtered back projection (FBP), shown in Fig. 7c, with interpolation for an equal sized image as for wavelet based reconstruction. The differences between the wavelet based reconstruction and traditional filtered back projection are evaluated using the reconstructed profiles at an arbitrarily chosen row. For the sake if illustration, the 80th horizontal row of pixels (40 mm at y axis) and 80th vertical column of pixels (40 mm at x axis) are chosen for illustration in Figs. 7d and 7e. It is clear that there is almost no difference in the detected hole positions using either the wavelet version of reconstruction (dash line) or the traditional FBP algorithm (dash dot line).

5.2. Local reconstruction at centre area

Fig. 8 shows reconstructed images centred at a radius of 16 pixels using the local reconstruction method outlined in Section 4.2 and the traditional FBP algorithm. Fig. 8a is the local reconstruction after extrapolation from wavelet and scaling filtered projection, with downsampling, and the corresponding relative reconstruction error of 26%. Fig. 8b shows four subimages reconstructed from wavelet and scaling coefficients after constant extrapolation and BP. A local reconstruction of the ROI using FBP is achieved in Fig. 8c for comparison, which results in a bigger relative error proportional to the wavelet based error calculation (with a ratio of $3/5.2 = 0.58$), since the main difference in the amount of non-local data ($r_e - r_i$) for the two methods is small enough to be ignored. Figs. 8d and 8e show the reconstruction profiles at the 12th horizontal row (6 mm at y axis) and vertical column of pixels (6 mm at x axis) corresponding to each reconstruction.

5.3. Local reconstruction at off-centre area

Figs. 9a–9e show reconstructed images at an off-centre area with a radius of 61 pixels using the current local reconstruction method and the traditional FBP algorithm. Each of the subfigures illustrates, for comparison, local reconstruction
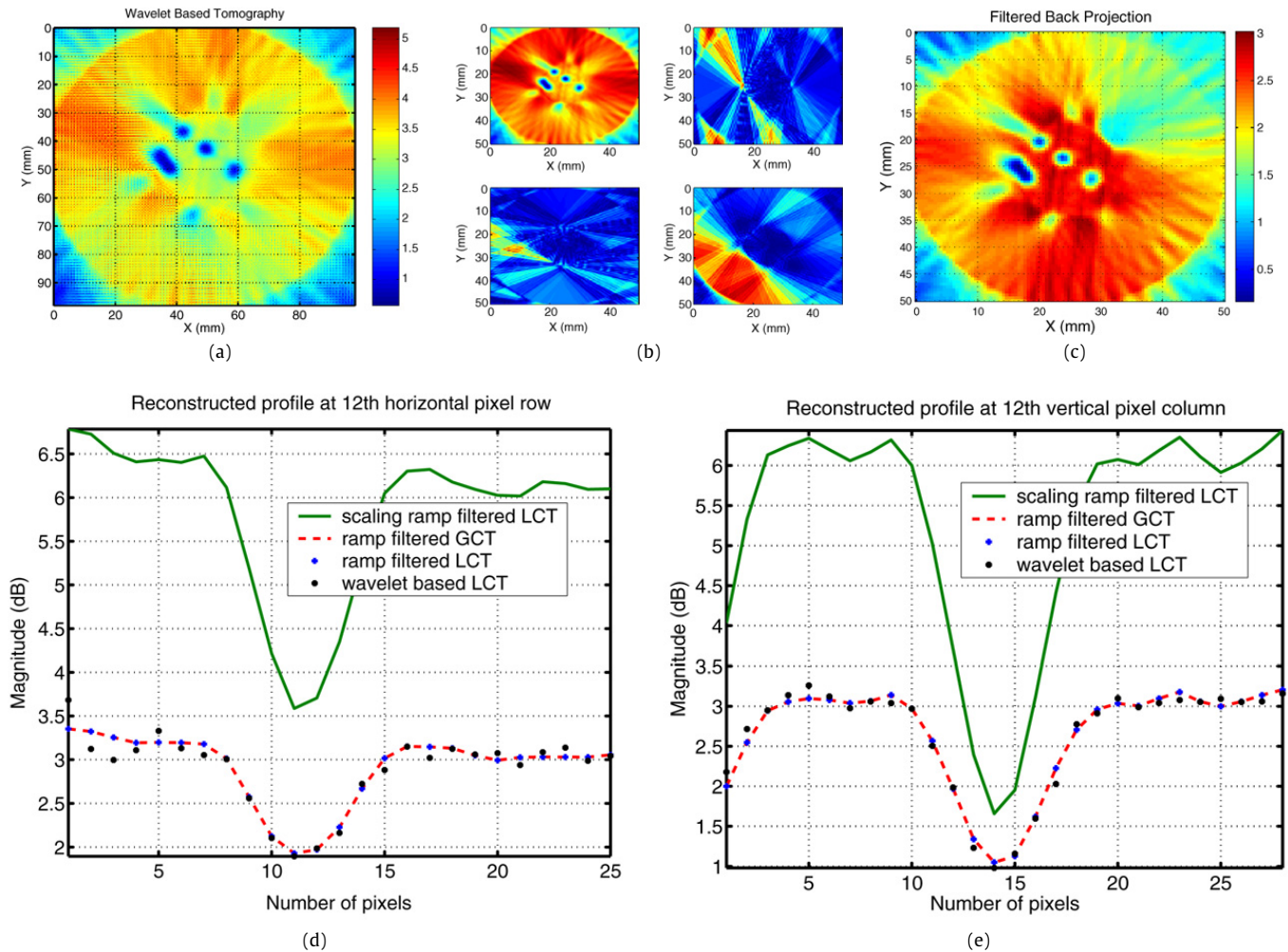
Fig. 8. (a) Reconstructed image localised to a centred region of interest from the inverse wavelet transform. (b) Centred approximate and three detail reconstruction subimages along clockwise direction. (c) A 196 × 196 pixel centred image of the polystyrene is reconstructed using traditional filtered back projection. (d) Reconstructed profiles at the 12th row (6 mm at y axis). (e) Reconstructed profiles at the 12th column (6 mm at x axis).

from extrapolated wavelet and scaling filtered projection after decomposition; the reconstruction of four subimages from extrapolated approximate and detail coefficients after BP; traditional FBP used for local reconstruction; the reconstruction profiles at the 28th horizontal row of pixels (14 mm at y axis) and the 12th vertical column of pixels (6 mm at y axis) are illustrated in Figs. 9d and 9e, both of which correspond to the reconstructions from approximate wavelet coefficients, FBP based local and global recovery in the ROI. The reconstruction from wavelet approximate coefficients shows strong contrast in intensity for different media and FBP based local reconstruction shows a little higher intensity than FBP based global reconstruction. The current image reconstruction is achieved using our algorithm with a relative reconstruction error of 24%.

6. Conclusion

We have shown an algorithm capable of reconstructing the wavelet and scaling coefficients of a function from its Radon transform of terahertz signals. Based on the observation that for some wavelet bases, with sufficient zero moments, the scaling and wavelet functions have essentially the same support after ramp filtering. An upper bound for the local reconstruction error is obtained in terms of the amount of non-local data which is used in the reconstruction scheme. In the experiments, an object is successfully recovered from terahertz measurements, which demonstrates the effectiveness of the current local reconstruction method based on wavelet techniques.

The reported relative error results is a little high, and it should be a priority to improve the estimate of this. As the current relative error calculation is based on the approximate image only, evaluation of the recovered image from approximate and detailed coefficients can lead to a more accurate estimate. In addition, since the current work involves only the one level of 2D DWT, it will be interesting to explore the reconstruction algorithm with more levels of decomposition. It is expected that the use of more levels of DWT will lead to improved performance at the expense of increased computational complexity. Moreover, a research area of much current interest is the development of statistical based local tomography algorithm and techniques [8,13]. In this framework, the tomographic reconstruction from partial data is formulated as a sta-
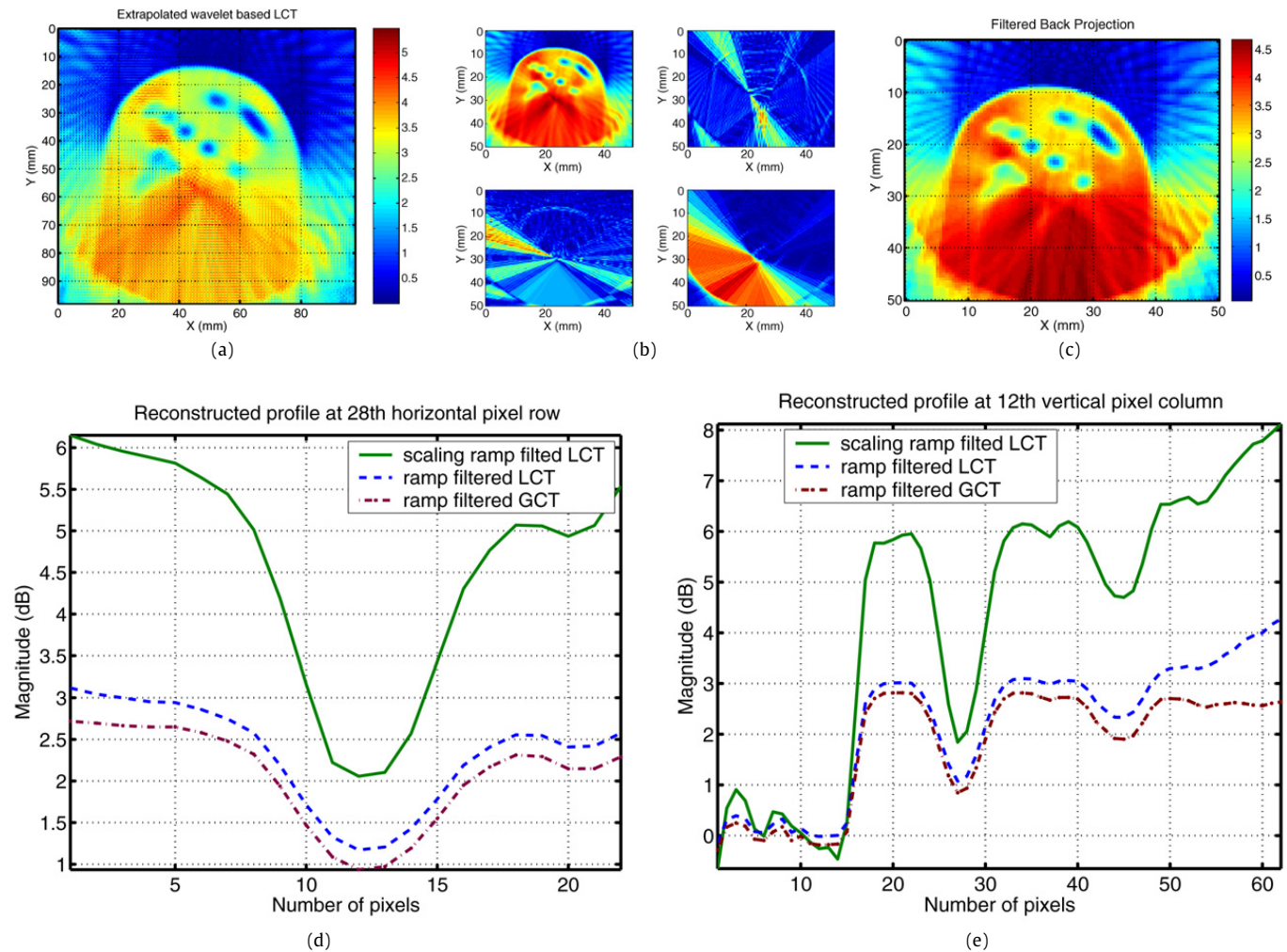
Fig. 9. (a) A reconstructed image from the inverse wavelet transform without decomposition for clarity. (b) Off-centred approximate and three detail reconstructed subimages along clockwise direction. (c) A FBP based local reconstruction at centred area. (d) Reconstructed profiles at the 28th row (14 mm at *y* axis). (e) Reconstructed profiles at the 12th column (6 mm at *x* axis).

tistical estimation problem. It is believed this framework matches well with our aim improving the localised reconstruction from our terahertz measurements.

References

[1] C. Berenstein, D. Walnut, Local inversion of the Radon transform in even dimensions using wavelets, in: 75 Years of Radon Transform, International Press, 1994, pp. 38–58.

[2] P.S. Carney, E. Wolf, G.S. Agarwal, Diffraction tomography using power extinction measurements, J. Opt. Soc. Am. A Opt. Vision 16 (11) (2002) 2643–2648.

[3] A.H. Delaney, Y. Bresler, Multiresolution tomographic reconstruction using wavelets, IEEE Trans. Image Process. 4 (6) (1995) 799–813.

[4] T.D. Dorney, W.W. Symes, R.G. Baraniuk, D.M. Mittleman, Terahertz multistatic reflection imaging, J. Opt. Soc. Am. A 19 (2002) 1432–1442.

[5] B. Ferguson, S. Wang, D. Gray, D. Abbott, X.C. Zhang, T-ray computed tomography, Opt. Lett. 27 (15) (2002) 1312–1314.

[6] B. Ferguson, S. Wang, D. Gray, D. Abbott, X.C. Zhang, Toward functional 3D T-ray imaging, Phys. Med. Biol. (IOP) 47 (2002) 3735–3742.

[7] R.C. Gonzalez, R.E. Woods, Digital Image Processing, Prentice–Hall, Inc., New Jersey, 2002.

[8] K.M. Hanson, G.W. Wecksung, Bayesian estimation of 3-D objects from few radiographs, J. Opt. Soc. Am. 73 (11) (1983) 1501–1509.

[9] B.B. Hu, M.C. Nuss, Imaging with terahertz waves, Opt. Lett. 20 (1716) 1995.

[10] Z. Jiang, X.-C. Zhang, Electro-optic measurement of THz field pulses with a chirped optical beam, Appl. Phys. Lett. 72 (16) (1998) 1945–1947.

[11] Z. Jiang, X.-C. Zhang, Single-shot spatiotemporal terahertz field imaging, Opt. Lett. 23 (14) (1998) 1114–1116.

[12] A.C. Kak, M. Slaney, Principles of Computerized Tomographic Imaging, IEEE Press, New York, 1988.

[13] V. Kolehmainen, S. Siltanen, S. Järvenpää, J.P. Kaipio, P. Koistinen, M. Lassas, J. Pirttilä, E. Somersalo, Statistical inversion for medical X-ray tomography with few radiographs. II. Application to dental radiology, Phys. Med. Biol. 48 (2003) 1465–1490.

[14] S. Mallat, A Wavelet Tour of Signal Processing, Academic Press, San Diego, CA, 1999.

[15] D. Mittleman, R. Neelamani, R.G. Baraniuk, J.V. Rudd, M. Koch, Recent advances in terahertz imaging, Appl. Phys. B 68 (1999) 1085–1094.

[16] K.L. Nguyen, M.L. Johns, L. Gladden, C.H. Worrall, P. Alexander, H.E. Beere, M. Pepper, D.A. Ritchie, J. Alton, S. Barbieri, E.H. Linfield, Three-dimensional imaging with a terahertz quantum cascade laser, Opt. Express 14 (6) (2006) 2123–2129.

[17] F. Rashid-Farrokhi, K.J.R. Liu, C.A. Berenstein, D. Walnut, Wavelet-based multiresolution local tomography, IEEE Trans. Image Process. 6 (10) (1997) 1412–1430.

[18] A.B. Ruffin, J. Van Rudd, J. Decker, L. Sanchez-Palencia, L. Le Hors, J.F. Whitaker, T.B. Norris, Time reversal terahertz imaging, IEEE J. Quant. Electron. 38 (8) (2002) 1110–1119.

[19] E.B. Treacy, Optical pulse compression with diffraction gratings, IEEE J. Quant. Electron. 5 (9) (1969) 454–458.

[20] S. Wang, B. Ferguson, D. Gray, D. Abbott, X.C. Zhang, T-ray imaging and tomography, J. Biol. Phys. 29 (2003) 247–256.

[21] S. Wang, B. Ferguson, X.-C. Zhang, Pulsed terahertz tomography, J. Phys. D: Appl. Phys. 37 (2004) R1–R36;
see also Erratum: S. Wang, B. Ferguson, X.-C. Zhang, J. Phys. D: Appl. Phys. 37 (2004) 964.

[22] X.-X. Yin, Brian W.-H. Ng, B. Ferguson, S.P. Mickan, D. Abbott, 2-D wavelet segmentation in 3-D T-ray tomography, IEEE Sens. J. 7 (3) (2007) 342–343.

[23] H. Zhong, J.Z. Xu, X. Xie, T. Yuan, R. Reightler, E. Madaras, X.-C. Zhang, Nondestructive defect identification with terahertz time-of-flight tomography, IEEE Sens. J. 5 (2) (2005) 203–208.

Xiaoxia (Sunny) Yin (S'07) was born in Dalian, China. She received the BEng degree in Industrial Electronics from Dalian University, Liaoning, PR China, and is currently working toward the PhD degree on three dimensional terahertz computed tomography under Derek Abbott and Brian Ng. Her research interests include multiresolution analysis, segmentation, image reconstruction and classification, and their applications to T-ray imaging. Presently in 2008, she is a visiting scholar at the University of Reading, UK, under Silas Hadjiloucas and at the University of Cambridge, UK, under Lynn F. Gladden.

Ms Yin received a series of awards, including the PhD Scholarship of The University of Adelaide (2005), WavE Travel Fellowship from Switzerland (2006), The International Association for Pattern Recognition (IAPR) travel stipend from Hong Kong (2006), Research Abroad Scholarship from The University of Adelaide (2006), the Roger Pysden Memorial Fellowship from Australia Business, ABL State Chamber (2006), a student scholarship from 2007 IEEE International Symposium on Industrial Electronics in Vigo, Spain (2007), a Mutual Community Postgraduate Travel Grant from the University of Adelaide (2007), and an Overseas Travel Fellowship from The Australian Research Council Nanotechnology Network (ARCNN) (2007).

Brian W.-H. Ng (S'97–M'02) was born in Mid-level, Hong Kong, on May 12, 1974. He received a BSc in Mathematics and Computer Science in 1996. In 1997, he received a BEng (Hons) and, in 2003, a PhD under Abdelsalam Bouzerdoum both in Electrical and Electronic Engineering from the University of Adelaide, Australia. During his studies, he was awarded the University of Adelaide medal for the top graduate in Electrical and Electronic Engineering. Since 2002, he has been a Lecturer at the University of Adelaide in the School of Electrical and Electronic Engineering. His research interests include signal processing, bio-inspired engineering, distributed sensor networks, software defined radio, as well as signal processing for T-ray imaging.

Dr Ng is currently an active member within the South Australian chapter of the IEEE and is a Member of the IEEE.

Bradley Ferguson (S'00–M'04) was born on August 8, 1975, in Freemantle, Western Australia, and graduated from The University of Adelaide with a BEng in Electrical and Electronic Engineering, 1997. He then worked for Vision Abell Pty Ltd for three years before returning to The University of Adelaide. There, in 2005, he received a PhD (with Special Commendation) in the area of T-ray image processing under Derek Abbott and Douglas A. Gray. In 2001 he was awarded a Fulbright Scholarship, and spent two years collaborating at X.-C. Zhang's group at Rensselaer Polytechnic Institute in Troy, NY, USA. He has won a number of honors and awards including South Australian Employers' Chamber Prize in Electronic Engineering (1996), Institution of Radio and Electronics Engineer Prize in Microelectronics (1997), Philips Industries Holdings Ltd Prize in Electronics (1997), South Australian Premier's Scholarship (1999), Australian Postgraduate Award (APA) scholarship (1999), Mutual Community Postgraduate Scholarship (2000), D.R. Stranks Postgraduate Scholarship (2000), Brenda Nettle Graduate Student Award (2003), New Focus Graduate Student Award (2003), University Alumni Medal (2005), The Gertrude Rohan Prize in Electronics (2006), and a Tall Poppy Award for science (2006).

Bradley Ferguson was the President of The University of Adelaide student chapter of the IEEE (2000–2001) and is the South Australian State Secretary of Fulbright Alumni Association (2004–present). He is a member of the SPIE, IEEE, LEOS, OSA. His current research interests include THz-TDS and RF photonics. Dr Ferguson is currently an Adjunct Senior Lecturer at The University of Adelaide and is concurrently employed by the Electronic Warfare Division of Tenix Systems Pty Ltd, Australia.

Derek Abbott (M'85–SM'99–F'05) was born on May 3, 1960, in South Kensington, London, UK, and he received a BSc (Hons) in physics (1982) from Loughborough University of Technology, UK. He completed his PhD (with commendation), in electrical and electronic engineering (1995) from The University of Adelaide, Australia, under Kamran Eshraghian and Bruce R. Davis. He has led a number of research programs in the imaging arena, ranging from the optical to infrared to millimeter wave to T-ray (terahertz gap) regimes. From 1978 to 1986, he worked at the GEC Hirst Research Centre, London, UK, in the area of visible and infrared image sensors. His expertise also spans VLSI design, optoelectronics, device physics, and noise; where he has worked with nMOS, CMOS, SOS, CCD, GaAs, and vacuum microelectronic technologies. On migration to Australia, he worked for Austek Microsystems, Technology Park, South Australia, in 1986. Since 1987, he has been with The University of Adelaide, where he is presently a full Professor in the School of Electrical and Electronic Engineering and the Director of the Centre for Biomedical Engineering (CBME). He has appeared on national and international television and radio and has also received scientific reportage in New Scientist, The Sciences, Scientific American, Nature, The New York Times, and Sciences et Avenir. He holds over 300 publications/patents and has been an invited speaker at over 80 institutions, including Princeton, NJ; MIT, MA; Santa Fe Institute, NM; Los Alamos National Laboratories, NM; Cambridge, UK; and EPFL, Lausanne, Switzerland. He won the GEC Bursary (1977), the Stephen Cole the Elder Prize (1998), the E.R.H. Tiekink Memorial Award (2002), SPIE Scholarship Award for Optical Engineering and Science (2003), the South Australian Tall Poppy Award for Science (2004) and the Premier's SA Great Award in Science and Technology for outstanding contributions to South Australia (2004). He has served as an editor and/or guest editor for a number of journals including *IEEE Journal of Solid-State Circuits*, *Chaos* (AIP), *Smart Structures and Materials* (IOP), *Journal of Optics B* (IOP), *Microelectronics Journal* (Elsevier), *Fluctuation Noise Letters* (World Scientific), and is currently on the Editorial Board of *Proceedings of the IEEE*. He has served on a number of IEEE technical program committees, including the IEEE APCCS and the IEEE GaAs IC Symposium. Professor Abbott is a Fellow of the Institute of Physics (IOP), with honorary life membership, and is a Fellow of the IEEE.